Paper 21

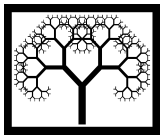

Proceedings of the Eighth International Conference
on Engineering Computational Technology,
B.H.V. Topping, (Editor),
Civil-Comp Press, Stirlingshire, Scotland

Application of Micromechanics in Engineering Practice

M. Šejnoha, V. Šmilauer, J. Němeček and L. Kopecký
Department of Mechanics, Faculty of Civil Engineering
Czech Technical University in Prague, Czech Republic

Abstract

Since learning from examples is the most simple way towards understanding, this paper may serve as a tutorial for the application of various averaging schemes to the derivation of effective properties of heterogeneous materials which show multiple scales. The simplicity and ease of use of analytical methods may play an enabling role in attracting young students and even engineers to the field of micromechanics by giving them the opportunity of directly applying the gained theoretical background to the solution of a variety of engineering problems. Several vastly dissimilar material systems are examined. In particular, the calculation of Young's modulus as a function of the degree of hydration of alkali-activated fly ash is discussed first followed by the application of micromechanical modeling to natural wood and closed with the reference to metallic foams. To show a common merit of individual materials the following topics will govern their analysis: a) identification of scales based on image analysis, b) identification of intrinsic material properties of individual phases based on nanoindentation, c) hierarchical homogenization employing the most suitable method on a given scale, d) corroborating theoretical predictions by experimental observations on the macro-scale.

Keywords: Mori-Tanaka method, self-consistent method, differential scheme, alcali activated fly ash, natural wood, metallic foam, image analysis, nanoindentation, multiscale homogenization.

1 Introduction

The field of composite materials now offers a tremendous variability and complexity of microstructures in dependence on their particular application. Nevertheless, it still shows a number of common features which bring various material systems to the same

footing at least from their analysis point of view. The latter issue has been repeatedly exploited particularly in connection with systems described by limited number of data often reduced to volume fractions and material properties of individual phases and assumptions of their statistically uniform arrangement [9, 2, 4].

Introduction of images of real microstructures into the analysis opened the way to more rigorous quantification of microstructures [15] as well as more advanced modeling strategies based on statistically equivalent representation of microstructural details by computational models [22, 17, 23] often formulated in the hierarchical manner to account for multiple scales [5, 14]. The use of advanced computational strategies was further supported by novel techniques such as nanoindentation [12, 11] for the determination of material properties of composite constituents on the level of microns. Note however that combining image analysis, nanoindentation and hierarchical modeling is by no means limited to complex and time consuming computations. By contrast, the use of analytical models such as Self-consistent [6] and Mori-Tanaka [1] methods is sufficient in many practical applications particularly if benefiting from the above three items. This last statement will be scrutinized hereinafter.

Since learning from examples is the most simple way towards understanding, and to further support an interdisciplinary character of the field of composites, we consider thorough evaluation of three, from the application point of view, vastly dissimilar material systems. Calculation of Young's modulus as a function of the degree of hydration of alkali-activated fly ash [19] is discussed next to the application of micromechanical modeling to natural wood [8] and metallic foams [12].

The remainder of the paper is structured as follows. Section 2 outlines material characterization adopting image analysis to identify individual scales and nanoindentation to derive local mechanical properties of individual phases. Application of the two basic averaging schemes in the light of multi-scale analysis is presented in Section 3. Summary of the advocated modeling strategy is finally provided in Section 4.

2 Material quantification

Application of simple averaging schemes, and the Mori-Tanaka method in particular, may cause certain complications when combining several phases of dissimilar shape and orientation at the same time, e.g. reinforcing inclusions and porosity. The two on the other hand often show obvious size differences which allows us to treat them on separate scales thus simplifying the analysis to two-phase systems only. This example is just one of many, as will be seen in Section 2.1, where image analysis proves useful in properly identifying the essential material length scales. Prediction of effective properties then typically relies on uncoupled "bottom-up" multi-scale analysis.

Regardless of number of scales, the local phase properties on the smallest scale are needed to perform the first homogenized step. In the present study such data are acquired with the help of nanoindentation examined in Section 2.2 as another tool for material characterization.

2.1 Identification of scales

This section summarizes the results of image analysis carried out at the Department of Mechanics, Faculty of Civil Engineering, Czech Technical University in Prague. In particular, Alkali-activated fly ash (AAFA), natural wood and metallic foam are considered in a sequel.

Alcali-activated fly ash The first example considers a low-calcium fly ash, class F, see e.g. [18] for more details. The back scattered electron (BSE) images of matured alkali-activated pastes taken by environmental scanning electron microscope (ESEM) for two particular samples cured at ambient ($\approx 25°$C) and high ($\approx 80°$C) temperatures appear in Figure 1. Clear morphological dissimilarities of the resulting microstructures linked to a particular curing step are easy to observe.

Regardless of the curing process, one may identify at least two distinct scales: the level of N-A-S-H gel and the level of paste. While the paste level is typically considered as a three-phase material system consisting of partly activated or nonactivated remainder of fly ash and compact glass particles (phase 1) and part of the open porosity filled with an activator in the form of evaporable water (phase 2) embedded into a N-A-S-H gel matrix (phase 3), the level of gel is decomposed into two phases of solid gel particles and the remainder of open porosity. However, it has been observed in [19] that for AAFA the entire open porosity can be assigned to the level of N-A-S-H gel, which allows us to treat the material at both levels as a two-phase composite.

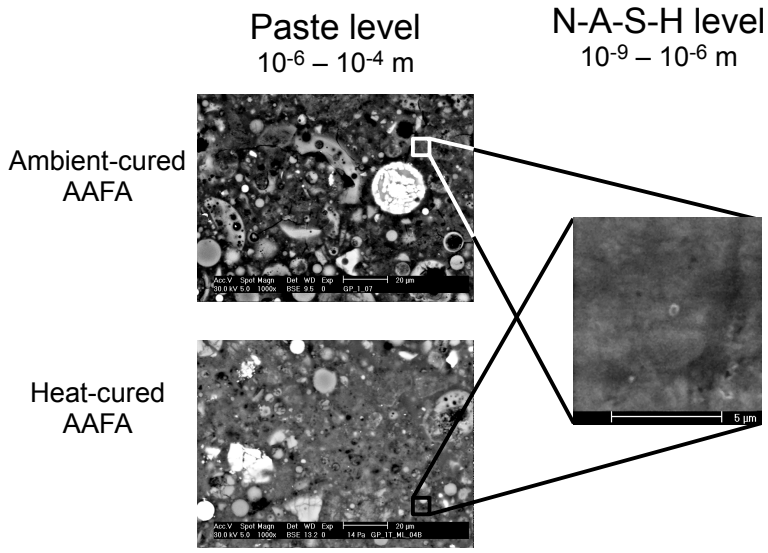

Figure 1: Representation of individual scales.The paste level displays BSE images of two microstructures from alkali-activated fly ash (AAFA, ambient and heat cured)

Natural wood Birch is considered in this paper as one particular representative of natural cellular materials of low relative density. It belongs to a group of hardwoods

with a typical microstructure seen in Figure 2. It consists of hollow 10 – 30 μm wide and 3-7 mm long tubes (cells) called tracheids and larger cells called vessels. Vessels are used to carry water up the tree, they are much wider than tracheids and may extend for several meters.

These basic features of wood microstructure help us to identify four distinct scales also shown in Figure 2. Clearly, on every scale the composite can be considered as a two-phase system with a certain homogenized matrix derived from the homogenization step performed on a lower scale.

If zooming in on the cell wall we recognize several sequentially deposited layers building up the wall. About 80 – 90% of the total cell wall thickness is taken by the secondary layer 2 (S2), which is the major contributor to the mechanical properties of wood cell walls. On the inner side of the wall we identify the compound middle lamella (CML) connecting the wood cells, the primary layer (P) and the secondary layer 1 (S1), while on the outer side we encounter the tertiary layer (T). The material species found within individual layers can be assumed tissue independent, universal to all woods. In [8] the authors considered further downscaling into the cell-wall level. Here, we examine the possibility of replacing the heterogeneous cell wall by equivalent properties provided directly by nanoindentation. This approach thus reduces the proposed multi-scale scheme again to a two-step homogenization considering only the level of tracheids and the level of vessels.

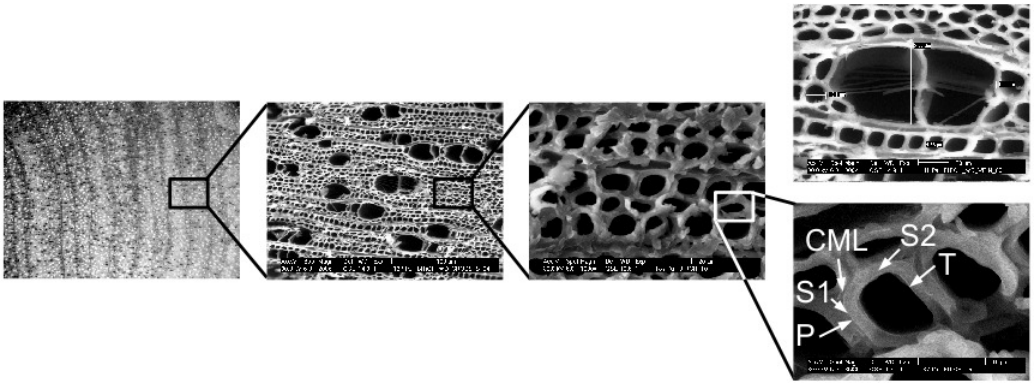

Figure 2: Representation of scales. From the left - macro-scale RVE of birch cross-section, ESEM image of meso-scale dominated by large vessels, ESEM image of meso-scale dominated by tracheids, ESEM image of cell wall identifying individual layers (micro-scale)

Metallic foam A lightweight aluminium foam is another example of highly porous materials. While a cellular microstructure of closed cell metallic foams can be seen as a link to a natural wood discussed previously their internal porosity, often exceeding 90%, is considerably higher making foams again a unique example for testing adequacy of averaging schemes in similar applications.

A hierarchy of microstructures typical of closed cell foams, identifying two par-

ticular scales of interest be subject to homogenization, is seen in Figure 3(a). From the micromechanics point of view, the metallic foam resembles a composite made of a metal matrix weakened by randomly distributed ellipsoidal voids. If further zooming into the aluminium wall we observe one additional two-phase material consisting of Al-rich areas (dark zone) and Ca/Ti-rich area (light zone). While the Al-rich zone consists mainly of aluminium and aluminium oxide, the Ca/Ti-rich contains apart from the previous two components non-negligible traces of calcium and titanium, see [12] for details.

Once knowing the volume fractions of both phases, estimated for example from the binary counterparts of original images, the overall properties can be once again predicted from a two-step analysis first homogenizing the scale of a cell wall followed by the homogenization of a porous foam.

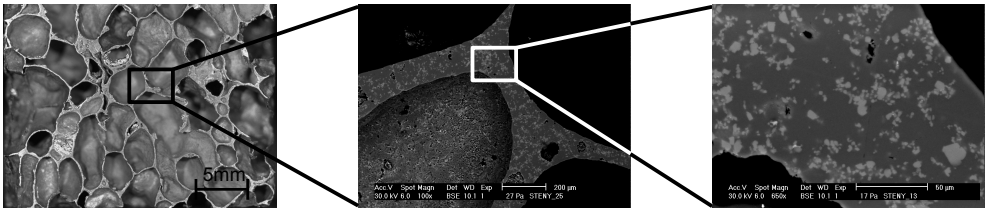

Figure 3: Representation of individual scales. From the left - image of a metallic foam structure, ESEM image of a cell wall, detailed ESEM image of a cell wall showing Al-rich (dark zone) and Ca/Ti-rich (light zone) areas

2.2 Identification of intrinsic material properties

Prediction of complex macroscopic response of highly heterogeneous materials from local phase constitutive theories is a formidable aspect of micromechanical modeling. However, the reliability of these predictions is considerably influenced by available information on material data of individual constituents. At present, nanoindentation is the only experimental technique that can be used for a direct measurement of mechanical properties at material micro-level. However, it goes beyond the present scope to discuss the details of this measuring technique. We therefore refer the interested reader to [11, 13, 12, to cite a few] and limit our attention only to the results pertinent to the selected three systems, particularly in the light of the expected hierarchical modeling.

Alcali-activated fly ash We begin by noting that the area affected by nanoindentation amounts to about $3\times$ the depth of indents, which ranged from 100 nm to 400 nm in this particular case [13] (the scale of N-A-S-H gel according to Figure 1). Such an area thus embraces majority of all pores. The elastic modulus estimated from nanoindentation must therefore be understood in a sense of a homogenized quantity of a two-phase composite collecting both the solid gel particles and open porosity.

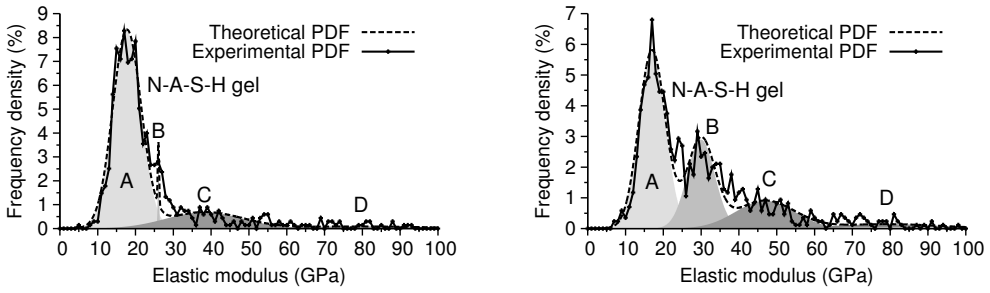

Figure 4: Results of deconvolution algorithm: (a) ambient-cured AAFA, (b) heat-cured AAFA

Figure 4 shows distributions of the elastic moduli of principal phases derived from 700 indents. It clearly identifies the influence of curing step on the microstructure heterogeneity. The results corresponding to particular time of indentation (98 days for both ambient-cured (DoR$\approx$0.44) and heat-cured (DoR$\approx$1) samples, see Section 3 for DoR (degree of reaction) identification) are listed in Table 1 together with associated volume fractions. How the volume fractions can be related to the time of indentation will be briefly discussed in the next section. Further details are available in [19].

Phase	Heat cured	Ambient cured
A. N-A-S-H gel	17.03 ± 3.48 (50.7%)	17.72 ± 3.75 (77.5%)
B. Partly-activated slag	29.95 ± 3.66 (26.6%)	26.06 ± 0.18 (1.1%)
C. Nonactivated slag	46.9 ± 7.76 (17.6%)	38.27 ± 10.13 (17.5%)
D. Nonactivated compact glass	79.15 ± 14.34 (5.1%)	79.65 ± 16.99 (3.9%)

Table 1: Phase volume fractions in [%] and elastic moduli in [GPa] of AAFA from deconvolution of indentation results [13]

Natural wood Suppose that the equivalent material properties below the cell level can be extracted from nanoindentation data. In such a case the prediction of macroscopic properties simplifies to a two-step homogenization of a two-phase porous system where inclusions would be well approximated by a hollow cylinder with a circular cross-section. One particular loading diagram is shown in Figure 5(b). Ten such indents were made in the S2 layer to render the mean value of Young's modulus in the longitudinal direction equal to 11.8 MPa.

However, this value considerably deviates from the one provided by analytical homogenization that consideres the tissue-independent wood species observed below the cell wall level [7]. This can be attributed to the intrinsic anisotropy of cell walls driven by the orientation of microfibrils of the crystalline cellulose and the loading angle of the Berchovich tip as seen in Figure 5(a). Obvious thought thus would be to exploit the nanoindentation results in estimation of the microfibrils angle (MFA) as outlined in the next section.

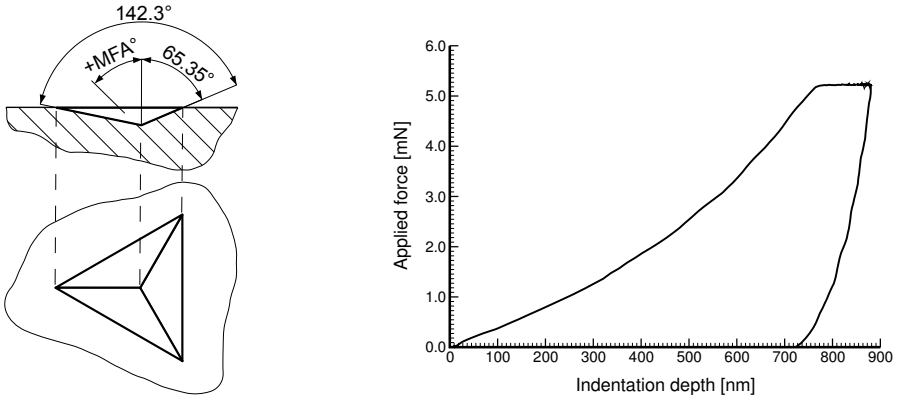

(a) (b)

Figure 5: (a) Orientation of the loading angle of the Berchovich tip with respect to a microfibril angle, (b) Loading diagram

Metallic foam The results from nanoindentation tests are plotted in Figure 6 showing on the right a typical loading diagram for each phase. Two hundred indents were considered in two selected regions covered by a 10×10 loading pattern with a 10 μm spacing between individual indents. The results of statistical analysis are seen in Figure 6(a).

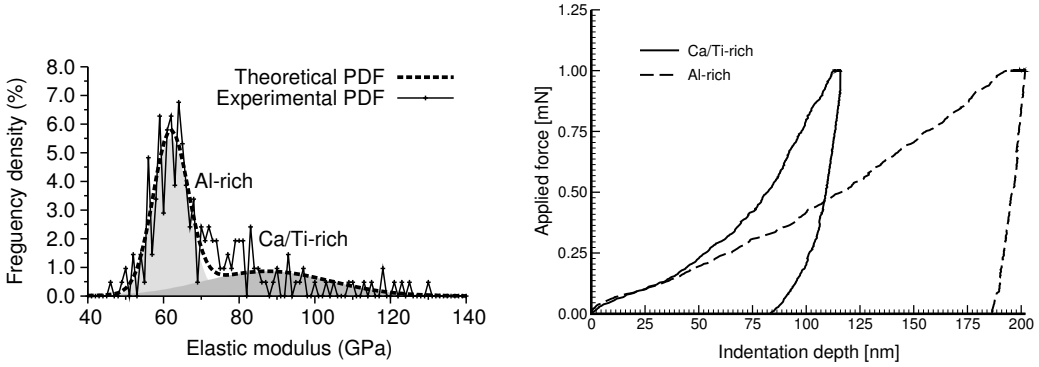

(a) (b)

Figure 6: (a) Deconvoluted phases identifying one dominant Al-rich and one minor Ca/Ti-rich phases, (b) Loading diagrams for Al-rich and Ca/Ti-rich zones

A relatively high scatter of the measurements pertinent to the Ca/Ti-rich phase can be attributed to a considerable variation in the area of isolated light zones, which might not be sufficiently large to comply with the theoretical assumption of the elastic subspace [12]. Notice also much larger standard deviation for the Ca/Ti-rich phase in comparison to the Al-rich phase in Table 2 listing also the associated mean values of the elastic moduli and the estimated volume fractions of both phases.

Phase	Mean [GPa]	Standard deviation [GPa]	Volume fraction [-]
Al-rich	61.9	4.6	0.64
Ca/Ti-rich	87.4	16.7	0.36

Table 2: Phase volume fractions and elastic moduli from deconvolution [12]

3 Effective properties from hierarchical modeling

This section is concerned with the application of simple averaging techniques to the evaluation of effective elastic properties of the selected material systems. From the homogenization point of view it is sufficient to consider the following four material systems:

1. isotropic matrix reinforced by transversely isotropic cylindrical fibers,

2. transversely isotropic matrix reinforced by cylindrical pores,

3. isotropic matrix reinforced by randomly distributed isotropic spherical particles or more generally a two-phase systems where both phases are assumed spherical and isotropic,

4. isotropic matrix reinforced by randomly distributed isotropic spherical pores.

The Self-consistent, Mori-Tanaka and differential schemes were adopted in this study at some point of the multi-scale homogenization approach. These methods are briefly summarized hereinafter. We limit our attention only to their specific formats pertinet to the above material systems where applicable:

- The **Self-consistent method** for a two-phase composite system where both phase are isotropic of a spherical shape provides the effective bulk and shear moduli ($K^{\mathrm{SC}}, G^{\mathrm{SC}}$) by solving the following set of implicit equations

$$\frac{c_1 K_1}{3K_1 + 4G^{\mathrm{SC}}} + \frac{c_2 K_2}{3K_2 + 4G^{\mathrm{SC}}} = \frac{K^{\mathrm{SC}}}{3K^{\mathrm{SC}} + 4G^{\mathrm{SC}}}, \tag{1}$$

$$\frac{c_2 G_1}{G^{\mathrm{SC}} - G_1} + \frac{c_1 G_2}{G^{\mathrm{SC}} - G_2} = -\frac{2}{5} - \frac{3K^{\mathrm{SC}}}{5(3K^{\mathrm{SC}} + 4G^{\mathrm{SC}})}, \tag{2}$$

  where K_r, G_r, c_r are the phase bulk and shear moduli and volume fraction, respectively.

- Application of the **Mori-Tanaka method** to a two-phase system consiting of a traneversely isotropic matrix reinforced by transversely isotropic fibers having circular cross-section leads to the following set of equations written here in

terms of Hill's moduli [3]

$$
\begin{aligned}
\mathrm{k}^{\mathrm{MT}} &= \frac{\mathrm{k}_2\mathrm{k}_1 + \mathrm{m}_1\left(c_2\mathrm{k}_2 + c_1\mathrm{k}_1\right)}{c_2\mathrm{k}_1 + c_1\mathrm{k}_2 + \mathrm{m}_1}, \\
l^{\mathrm{MT}} &= \frac{c_2 l_2\left(\mathrm{k}_1 + \mathrm{m}_1\right) + c_1 l_1\left(\mathrm{k}_2 + \mathrm{m}_1\right)}{c_2\left(\mathrm{k}_1 + \mathrm{m}_1\right) + c_1\left(\mathrm{k}_2 + \mathrm{m}_1\right)}, \\
\mathrm{n}^{\mathrm{MT}} &= c_2\mathrm{n}_2 + c_1\mathrm{n}_1 + \left(l - c_2 l_2 - c_1 l_1\right)\frac{l_2 - l_1}{\mathrm{k}_2 - \mathrm{k}_1}, \\
\mathrm{m}^{\mathrm{MT}} &= \frac{\mathrm{m}_2\mathrm{m}_1\left(\mathrm{k}_1 + 2\mathrm{m}_1\right) + \mathrm{k}_1\mathrm{m}_1\left(c_2\mathrm{m}_2 + c_1\mathrm{m}_1\right)}{\mathrm{k}_1\mathrm{m}_1 + \left(\mathrm{k}_1 + 2\mathrm{m}_1\right)\left(c_2\mathrm{m}_1 + c_1\mathrm{m}_2\right)}, \\
\mathrm{p}^{\mathrm{MT}} &= \frac{2c_2\mathrm{p}_2\mathrm{p}_1 + c_1\left(\mathrm{p}_2\mathrm{p}_1 + \mathrm{p}_1^2\right)}{2c_2\mathrm{p}_1 + c_1\left(\mathrm{p}_2 + \mathrm{p}_1\right)}.
\end{aligned}
\tag{3}
$$

To arrive at a porous system it is sufficient to remove the material constants corresponding to the fiber phase 2; c_2 then represents the volume fraction of pores. For a two-phase system where the isotropic matric is reinforced by randomly distributed spherical particles the Mori-Tanaka method yields the effective bulk and shear moduli $(K^{\mathrm{MT}}, G^{\mathrm{MT}})$ in the form

$$
K^{\mathrm{MT}} = K_1\left(1 + \frac{c_2(K_2 - K_1)}{K_1 + (1 - c_2)\xi_1(K_2 - K_1)}\right), \tag{4}
$$

$$
G^{\mathrm{MT}} = G_1\left(1 + \frac{c_2(G_2 - G_1)}{G_1 + (1 - c_2)\eta_1(G_2 - G_1)}\right), \tag{5}
$$

where ξ_1, η_1 are written in terms of the matrix bulk and shear moduli of the matrix phase K_1, G_1 as

$$
\xi_1 = \frac{3K_1}{3K_1 + 4G_1}\,, \qquad \eta_1 = \frac{6K_1 + 12G_1}{15K_1 + 20G_1}.
$$

The porous system can be addressed similalry as in the case of fibrous composite.

- When adopting the **Differential scheme** the estimates of the effective bulk and shear moduli $(K^{\mathrm{DS}}, G^{\mathrm{DS}})$ for the isotropic matrix wekened by spherical pores receive the form, see [24] for more details,

$$
\frac{G^{\mathrm{DS}}}{G_1} = (1 - f)^2\left[\frac{2(1 + \nu_1) + (1 - 5\nu_1)\left(\dfrac{G^{\mathrm{DS}}}{G_1}\right)^{3/5}}{3(1 - \nu_1)}\right]^{1/3}, \tag{6}
$$

$$
\frac{1}{K^{\mathrm{DS}}} = \frac{3}{4G^{\mathrm{DS}}}\left[1 + \frac{1 - 5\nu_1}{1 + \nu_1}\left(\frac{G^{\mathrm{DS}}}{G_1}\right)^{3/5}\right], \tag{7}
$$

where ν_1 is the Poisson ration of the matrix phase.

Alcali-activated fly ash In [19] the authors developed a volumetric model for alkali-activated aluminosilicate materials to describe the change of volume of phases evolving during reaction processes as a function of so called degree of reaction (DoR).

Without going into details we consider a two-step homogenization and write for the level of paste

$$1 = c_{FA} + c_{NASH}, \tag{8}$$

where c_{FA} and c_{NASH} stand for the volume fraction of nonactivated material and the volume fraction of N-A-S-H gel at the paste level. When moving down to the level of N-A-S-H gel we get

$$1 = c_{SGP}^{NASH} + c_{OP}^{NASH}, \tag{9}$$

$$c_{SGP}^{NASH} = \frac{c_{SGP}}{c_{NASH}}, \tag{10}$$

$$c_{OP}^{NASH} = \frac{c_{OP}}{c_{NASH}}. \tag{11}$$

where c_{SGP} and c_{OP} correspond to the volume fraction of the solid gel particles and open porosity, respectively. For DoR $= 0.44$, which corresponds to the date of indentation of ambient cured samples, the respective volume fractions are stored in Table 3.

Parameter	Calculated at $\mathrm{DoR} = 0.44$
c_{FA}	0.325
c_{SGP}	0.354
c_{OP}	0.321
c_{SGP}^{NASH}	0.525
c_{OP}^{NASH}	0.475

Table 3: Volume fractions of phases entering the volumetric model [19]

The intrinsic material properties used in homogenizaton are available in Table 4. Note that the intrinsic modulus of solid gel particles E_{SGP} was found from homogenization adopting the Mori-Tanaka method (Eqs. (4) - (5)) and the value of E_{NASH} measured by nanoindentation, recall Table 1.

Phase	Young's modulus [GPa]	Poisson ratio [-]
Fly ash	105	0.2
Open porosity	0.001	0.001
Solid gel particles	49.75	0.2

Table 4: Intrinsic elastic properties used in the homogenization [19, 10, 13]

We should point out a relatively high value of Young's modulus assumed for nonactivated particles on the paste level (Fly ash), which was found to deliver much better results in comparison to those derived from the homogenized value corresponding to nonactivated phases listed in Table 1. This can be attributed to the fact that even if an indented particle of a nonactivated phase has the size sufficiently exceeding the

affected volume (20-40 μm vs $3 \times 100 - 400$ nm), since being solitary, the measured value of the elastic modulus is significantly influenced by the surrounding material of more compliant N-A-S-H gel.

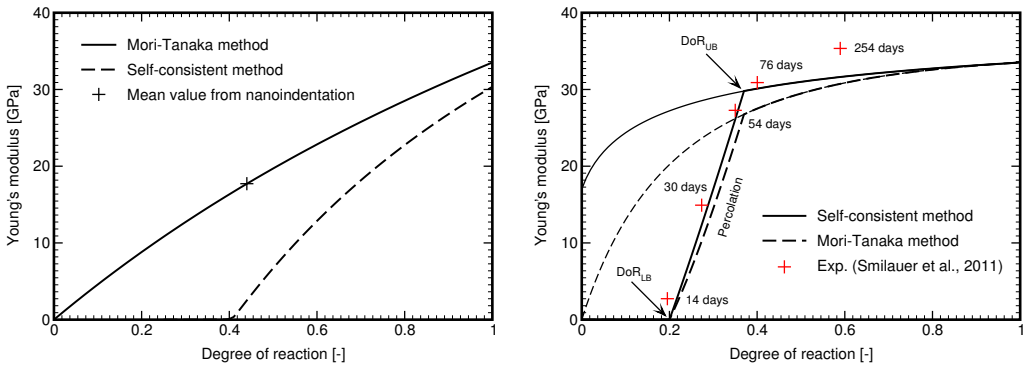

Figure 7: (a) Evolution of the homogenized Young's modulus as a function of DoR at the level of: (a) N-A-S-H gel, (b) Paste - percolation transition is bounded by lower DoR_{LB} and upper DoR_{UB} bounds

The results of a two-step multi-scale homogenization are evident in Figure 7. Figure 7(a) first displays evolution of the homogenized N-A-S-H gel elastic modulus as a function of DoR depicting also the matched measured value at DoR=0.44. These plots were found from Eqs. (1) - (2) and Eqs. (4) - (5). The results of the second homogenization step, where the nonactivated spherical particles (E_{FA}) are introduced into the homogenized N-A-S-H gel matrix, appear in Figure 7(b). These plots were obtained from the same equations as in the first homogenizations step on the level of N-A-S-H gel.

Note that the results provided by averaging schemes are valid for matured samples only. However, the available experimental data ($+$ sign in Figure 7(b)) indicate that a certain reaction time is needed for the gel to interconnect the unreacted material. This suggests introduction of a certain lower bound DoR_{LB} on the degree of reaction related to the percolation threshold. An associated upper bound DoR_{UB} is then assigned to DoR at the onset of maturity. A simple scaling factor p in the form

$$p = \frac{\mathrm{DoR} - \mathrm{DoR}_{LB}}{\mathrm{DoR}_{UB} - \mathrm{DoR}_{LB}}, \quad 0 \leq p \leq 1, \tag{12}$$

was introduced in [19] to interpolate between the two bounds. A relatively good match between experimental and homogenized values is a clear indication of the applicability of simple averaging schemes in this particular example.

Natural wood Section 2.2 already pointed out some complications in the determination of intrinsic material properties of the cell wall from nanoindentation owing to the uncertainty in the specification of loading angle directly from image analysis.

On the contrary, this value can be estimated when combining the results of analytical homogenization at the level of cell wall and nanoindetaion measurements.

To proceed we exploit the knowledge of tissue independent material data provided in [7], see Table 5, and set up a two-step homogenization scheme at the cell level.

Homogenization step	Phase	c_r [-]	$E_A(E)$ [GPa]	$G_A(G)$ [GPa]	$\nu_A(\nu)$ [-]	E_T [GPa]	G_T [GPa]
Step 1a	hemicellulose	0.55	8.1	3	0.33	-	-
2 phases	lignin	0.45	6	2.3	0.3	-	-
Step 1b	matrix (Step 1a)	0.65	7.1	2.7	0.33	-	-
3 phases	amorphous cell.	0.16	5.1	1.9	0.35	-	-
wall material	crystalline cell.	0.19	168	5.8	0	35	4.5

Table 5: Intrinsic material properties of the cell wall [7]

Homogenization of a wood cell wall with the mid-spam wall thickness of about 5 μm consideres, as siggested in [7], a three-phase composite consisting of cylindrical fiber-like aggregates of crystalline cellulose and of amorphous cellulose embedded into an isotropic polymer matrix. In this particular case the Mori-Tanaka method appears as a suitable choice for the derivation of the cell wall properties. If only one set of iclusions was present the system could be ellaborated with the help of Eqs. (3). However, a three-phase medium requires certain generalization as described, e.g. in [3]. This homogenization step is labeled as "Step 1b".

The homogenization "Step 1a" is reserved for the evaluation of effective properties of the matrix phase, which can be treated as suggested in [7] as another three-phase composite on the scale of nano-meters. At this level of magnification the authors treated all three phases on the same footing thus promoting the Self-consistent method as a suitable method of attack. For simplicity we neglect water and other wood extractives and consider hemicellulose and lignin only as two independent phases constituting the polymer matrix. This homogenization step thus calls for the application of Eqs. (1) - (2).

Combining the two steps yields the value of axial Young's modulus equal to 37.5 GPa essentially assuming the cell wall microfibrils be oriented in the longitudinal direction parallel to the direction of tracheids and vessels. Recall that the value of longitudinal Young's modulus provided by nanoindentation was equal to 11.8 GPa, which is less than half the value of the modulus estimated by homogenization. If we wish to link this discrepancy to the loading angle we first adopt standard transformation of coordinates and approximate the elastic moduli in the global coordinate system

by [1]

$$
\begin{aligned}
E_{11} \approx \frac{1}{M_{11}} &= \frac{\cos^4(\alpha)}{E_A} + \left(\frac{1}{G_A} - \frac{2\nu_A}{E_A}\right)\cos^2(\alpha)\sin^2(\alpha) + \frac{\sin^4(\alpha)}{E_T}, \\
E_{22} \approx \frac{1}{M_{22}} &= \frac{\sin^4(\alpha)}{E_A} + \left(\frac{1}{G_A} - \frac{2\nu_A}{E_A}\right)\cos^2(\alpha)\sin^2(\alpha) + \frac{\cos^4(\alpha)}{E_T}, \qquad (13) \\
G_{12} \approx \frac{1}{M_{66}} &= \left(\frac{1}{E_A} + \frac{1}{E_T} + \frac{2\nu_A}{E_A}\right)\sin^2(2\alpha) + \frac{\cos^2(2\alpha)}{G_A}.
\end{aligned}
$$

The results are plotted in Figure 8. If attributing the difference between theoretical and experimental values to the loading angle of the Berchovich tip only ($\alpha = 25^\circ$ for MFA of 0°) we see in Figure 8 that for 25° of MFA the value of longitudinal modulus provided by Eq. $(13)_1$ equals to 14.2 MPa.

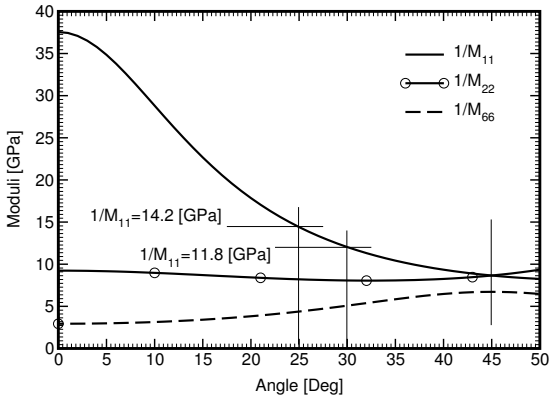

Figure 8: Effective wall properties as a function of the microfibrils angle

The next step would be to account for the wood anisotropy represented by MFA. Unfortunately, determination of the off-axis loading for a non-zero MFA is not trivial, since individual phases of the indenter will not form the same angle with respect to the alignment of microfibrils as evident from Figure 5(a). In [16] the authors addressed this issue by introducing an effective loading angle larger than, but clearly depending on, the actual MFA. Thus assuming for example the value of 20° suggests the value of microfibril angle of about 10° based on the nanoindentation data ($E_A = 11.8$ GPa, 30°), see Figure 8.

Completing the derivation of macroscopic properties requires application of modified Eqs. (3) again in two independent steps, first to consider a porous system composed of aligned cylindrical tracheids surrounded by a transversely isotropic matrix derived from the first homogenization step and second to account for larger cylindrical vessels.

[1] We consider only in-plane rotation trough angle α about the global $X_3 = x_3$ axis, the local x_1 axis is aligned with the direction of microfibrils.

Modulus [GPa]	MFA=0°	MFA=10°	Experiment [21]
E_{11}	16.6	11.6	15.3
E_{22}	1.6	1.5	1.0
G_{12}	0.8	0.9	1.1

Table 6: Effective elastic properties - summary

The final macroscopic predictions are summarized in Table 6. Supporting the theoretical predictions by available experimental data permits several general conclusions closing this section: a good potential of classical micromechanical models in applications covering a hierarchy of scales has been confirmed; proper identification of all important microstructural details is decisive for the success and reliability of final predictions; an independent experimental work on macro-scale must not be omitted.

Metallic foam This is the last example of a complex material system having a hierarchical microstructure. As expected, the prediction of effective properties can be performed again on two different scales.

It turns out that cell wall effective properties can be well approximated by the Self-consistent method when introducing the local phase properties and corresponding volume fractions from Table 2 into Eqs. (1) - (2). This gives the effective Young modulus and Poisson ratio equal to 70.1 and 0.35, respectively.

The second homogenization step is, however, much more complicated owing to the large porosity amounting to 91%. Suppose that the present material system can be modeled as a macroscopically isotropic porous medium with randomly distributed spherical voids. Inadequacy of the Self-consistent method in applications to porous media is clearly evident from plots in Figure 9(a). The Mori-Tanaka method (modified Eqs. (4) - (5)) on the other hand has been shown applicable in this case already in the previous example. The literature also offers many examples promoting the Differential scheme, Eqs. (6) - (7), as a suitable alternative.

The results plotted in Figure 9 suggest that unlike the Mori-Tanaka method, the Differential scheme performs relatively well particularly for higher porosity levels. This somewhat supports application of the Mori-Tanaka method for lower porosity wood samples. However, drawing such a conclusion from the study of one particular material system is precarious as suggested by experimental observations presented in [20] for a sintered glass containing spherical pores. These results promote on the other hand the Differential scheme for porosities below 50% while the Mori-Tanaka method for higher porosities, see Figure 9(b).

4 Conclusion

This paper was concerned with the application of simple micromechanical models in the framework of hierarchical modelling in vastly different areas of engineering

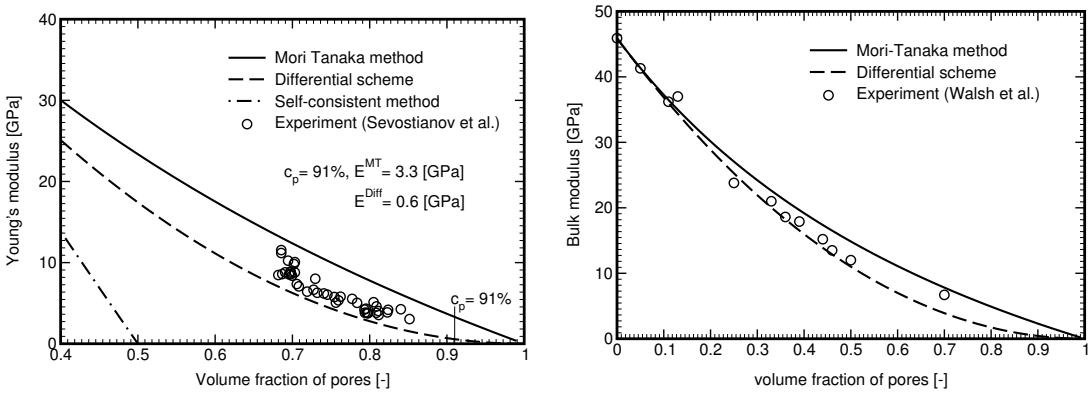

(a) (b)

Figure 9: Comparison between experimental measurements and predictions: (a) porous metallic foam, (b) sintered porous glass

interest. The preference has been given here to nanoindentation to determine phase properties, image analysis to determine phase volume fractions and basic averaging methods including the Mori-Tanaka, self-consitent and differential schemes to determine the effective properties. By discussing the quality of theoretical predictions in comparison with available experimental data we attempted to introduce the reader to the concept of a *virtual testing tool* as an integrated set of models, algorithms and procedures for the prediction of mechanical properties on an arbitrary scale.

Acknowledgments

The financial support by the GAČR grants 105/11/0224 and P105/12/0824 is gratefully acknowledged.

References

[1] Y. Benveniste, "A new approach to the application of Mori-Tanaka theory in composite materials", *Mechanics of Materials*, 6: 147–157, 1987.

[2] Y. Benveniste, G.J. Dvorak, T. Chen, "On diagonal and elastic symmetry of the approximate effective stiffness tensor of heterogeneous media", *Journal of the Mechanics and Physics of Solids*, 39(7): 927–946, 1991.

[3] T. Chen, G.J. Dvorak, Y. Benveniste, "Mori-Tanaka estimates of the overall elastic moduli of certain composite materials", *Journal of Applied Mechnaics*, 59: 539–546, 1992.

[4] G.J. Dvorak, Y. Benveniste, "On transformation strains and uniform fields in multiphase elastic media", *Proceedings of the Royal Society of London Series A - Mathematical, Physical and Engineering Sciences*, 437(1900): 291–310, 1992.

[5] J. Fish, K. Shek, "Multiscale Analysis of Large-Scale Nonlinear Structures and Materials", *International Journal for Computational Civil and Structural Engineering*, 1(1): 79–90, 2000.

[6] R. Hill, "A Self-consistent mechanics of composites materials", *Journal of the Mechanics and Physics of Solids*, 13: 213–222, 1965.

[7] K. Hofstetter, C. Hellmich, J. Eberhardsteiner, "Development and experimental validation of a continuum micromechanics model for the elasticity of wood", *European Journal of Mechanics - A/Solids*, 24(6): 1030–1053, 2005.

[8] K. Hofstetter, C. Hellmich, J. Eberhardsteiner, "Continuum micromechanics estimation of wood strength", *Proc. Appl. Math. Mech*, 6: 75–78, 2006.

[9] N. Laws, "The elastic response of composite materials", *Physics of Mechanics of Materials*, 1: 465–520, 1980.

[10] T. Matsunaga, J.K. Kim, S. Hardcastle, P.K. Rohatgi, "Crystallinity and selected properties of fly ash particles", *Materials Science and Engineering A*, 325(1-2): 333–343, 2002.

[11] J. Němeček, "Creep effects in nanoindentation of hydrated phases of cement pastes", *Material Characterization*, 60(9): 1028–1034, 2009.

[12] J. Němeček, V. Králík, J. Vondřejc, J. Němečeková, "Identification of micromechanical properties on metal foams using nanoindentation", in B. Topping, Y. Tsompanakis (Editors), *Proceedings of the Thirteenth International Conference on Civil, Structural and Environmental Engineering Computing*. Civil-Comp Press, 2011, on CD ROM, paper No. 125.

[13] J. Němeček, V. Šmilaurer, L. Kopecký, "Nanoindentation characteristics of alkali-activated aluminosilicate materials", *Cement & Concrete Composites*, 33: 163–170, 2011.

[14] J. Sýkora, T. Krejčí, J. Kruis, M. Šejnoha, "Computational homogenization of non-stationary transport processes in masonry structures", *Journal of Computational and Applied Mathematics*, 2011, Accepted.

[15] S. Torquato, G. Stell, "Microstructure of two-phase random media.I. The n-point probability functions", *Journal of Chemical Physics*, 77(4): 2071–2077, 1982.

[16] W.T.Y. Tze, S. Wang, T.G. Rials, G.M. Pharr, S.S. Kelley, "Nanoindentation of wood cell walls: Ccontinuous stiffness and hardness measurements", *Composites: Part A*, 38: 945–953, 2007.

[17] M. Šejnoha, J. Zeman, "Micromechanical modeling of imperfect textile composites", *International Journal of Engineering Science*, 46: 513–526, 2008.

[18] F. Škvára, L. Kopecký, V. Šmilauer, Z. Bittnar, "Material and structural characterization of alkali-activated low-calcium brown coal fly ash", *Journal of Hazardous Materials*, 168: 711–720, 2009.

[19] V. Šmilauer, P. Hlaváček, Škvára F., L. Kopecký, J. Němeček, "Micromechanical multiscale model for alkali activation of fly ash and metakaolin", *Journal of Material Sciece*, 46(20): 6545–6555, 2011.

[20] J.B. Walsh, W.F. Brace, A.W. England, "Effect of porosity on compressibility of glass", *Journal of the American Ceramic Society*, 48: 605–608, 1965.

[21] WHB, *Wood Handbook*, Forest Product Society, USA, 1999.

[22] J. Zeman, M. Šejnoha, "Numerical evaluation of effective properties of graphite fiber tow impregnated by polymer matrix", *Journal of the Mechanics and Physics of Solids*, 49(1): 69–90, 2001.

[23] J. Zeman, M. Šejnoha, "From random microstructures to representative volume elements", *Modelling and Simulation in Materials Science and Engineering*, 15 (4): S325–S335, 2007.

[24] R.W. Zimmerman, "Elastic moduli of a solid containing spherical inclusions", *Mechanics of Materials*, 12: 17–24, 1991.